Selective catalytic reduction of NO_x with NH_3 over short-range ordered W-O-Fe structures with high thermal stability

Ying Xin[1], Nana Zhang[1], Qian Li[1], Zhaoliang Zhang[1,*], Xiaoming Cao[2], Lirong Zheng[3], Yuewu Zeng[4], James A. Anderson[5,*]

[1] School of Chemistry and Chemical Engineering, Shandong Provincial Key Laboratory of Fluorine Chemistry and Chemical Materials, University of Jinan, Jinan 250022, China

[2] Center for Computational Chemistry, School of Chemistry and Molecular Engineering, East China University of Science and Technology, Shanghai 200237, China

[3] Institute of High Energy Physics, Chinese Academy of Sciences, Beijing 100049, China

[4] Center of Electron Microscopy and State Key Laboratory of Silicon Materials, Zhejiang University, Hangzhou 310027, China

[5] Surface Chemistry and Catalysis Group, Materials and Chemical Engineering, University of Aberdeen, AB24 3UE, United Kingdom

*Corresponding authors:

Zhaoliang Zhang: chm_zhangzl@ujn.edu.cn

James A. Anderson: j.anderson@abdn.ac.uk

Abstract

The selective catalytic reduction (SCR) of NO_x with NH_3 was studied over poorly-crystalline W-Fe composite oxides (W_aFeO_x). The short-range order present within the W-O-Fe structure was found to be responsible for the excellent SCR activity, in which the strong atomic-level interaction between Fe and W atoms promoted the formation of both Lewis and Brønsted acidity. The W-O-Fe structure existed as amorphous overlayers, approximately 2 nm thick over the surface of crystalline particles after high-temperature aging as shown by high-angle annular dark field scanning transmission electron microscopy (HAADF-STEM). After treatment at 800ºC for 5 h, the W_aFeO_x catalysts still showed almost 100% NO conversion in the range 300-450ºC with 100% N_2 selectivity, despite the loss in surface area. This resistance to the impacts of high temperature ageing guarantees high activity of SCR catalysts which often suffer during high-temperature excursions as in the case of diesel exhaust due to diesel particulate filter (DPF) regeneration.

Keywords: Nitrogen oxides; Selective catalytic reduction; Ammonia; Short-range order; High thermal stability

1. Introduction

Nitrogen oxides (NO_x, referring to NO and NO_2) are major air pollutants, which contribute to environmental issues such as acid rain, photochemical smog, atmospheric oxidant ozone increase and haze and harm human health [1, 2]. To reduce these effects, the removal of NO_x from anthropogenic sources including stationary (coal-fired power plants, etc.) and mobile sources (motor vehicles) is crucial. Selective catalytic reduction (SCR) of NO_x with NH_3 has proved to be an efficient means of reducing NO_x emission ($deNO_x$) [3-5]. V_2O_5-WO_3/TiO_2 is the most widely used NH_3-SCR catalyst, which has been commercialized for $deNO_x$. However, the disadvantages including the toxicity of vanadium, the narrow operational temperature window, and the deterioration of the structure and constituents after high-temperature aging, restricts its wider application [6, 7]. Development of new catalysts with improved NH_3-SCR performance and research on active site identification continues. Amorphous active catalysts/active species have attracted considerable attention due to their high activity.

As early as 1990s, the amorphous Cr_2O_3 catalyst was reported to exhibit superior SCR activity and N_2 selectivity compared to its crystalline counterpart [8, 9]. In 2007, Tang *et al.* found that the amorphous phase of MnO_x was much more active than its crystalline counterpart at low temperatures [10]. Similar phenomena were also found for composite oxides, for example, amorphous Mn and Ce species were thought to be responsible for SCR activity in Mn-supported TiO_2 [11, 12], and Ce-Ti mixed oxides [13-15], respectively. Significantly, the consensus for composite oxides is that short-range ordered structure is the location of as active sites, as in Fe-O-Ti [16-18], Ce-O-Ti [19], and Ce-O-W [20] systems, thereby highlighting the pivotal role of atomic-scale interaction.

It is well known that the amorphous structure is characterized by the absence of long-range order [21], which is metastable and readily transformed into the crystalline phase or is to phase separation after high-temperature treatment [22]. Both transformations generally lead to decreased SCR activity [10, 14]. For instance, during the diesel particulate filter (DPF) regeneration, the diesel exhaust gas temperature occasionally rises above 600°C, which may causes severe deactivation of V_2O_5-WO_3/TiO_2 catalysts [23]. Hence, the thermal stability of an SCR catalyst is crucial if it is to withstand such harsh environment. In this study, short-range ordered W-O-Fe active species in poorly-crystalline W-Fe composite oxides (W_aFeO_x) have been developed which exhibit excellent NH_3-SCR activity. Most importantly, the W-O-Fe structure was retained on the surface of a crystalline phase even after aging at 800°C for 5 h. Despite a significant loss in surface area, NO conversion in the range 300-450°C was close to 100% with 100% N_2 selectivity. These findings demonstrate the importance of fabrication of materials with short-range ordered W-O-Fe structure, which are highly dispersed at the outermost surface layer of crystallites after high-temperature and long-term operation.

2. Experimental

2.1 Sample preparation

The W_aFeO_x catalysts (with a W/Fe atomic ratio of *a*, ICP data) was prepared by a co-precipitation method using an aqueous solution of sodium tungstate ($Na_2WO_4 \cdot 2H_2O$, 200 mL) and ferrous sulfate ($FeSO_4 \cdot 7H_2O$, 100 mL) with ammonium hydroxide ($NH_3 \cdot H_2O$, 25-28 wt.%) at 35°C, with the pH of the precipitation process maintained above 6.0 and that of the resulting solution maintained at 9.0. The total amount of the metallic salt precursor was 0.03 mol. Ascorbic acid ($C_6H_8O_6$, 100 mg) was added to the initial iron precursor solution to mol.

ascorbic acid ($C_6H_8O_6$, 100 mg) was added to the initial iron precursor solution to enhance the reducibility of the Fe^{2+}. The obtained slurry was aged at 35°C with stirring for 3 h and subsequently filtrated and washed. The resulting solid was dried overnight at 70°C and calcined at 500°C (or 800°C) for 5 h. For comparison purposes, Fe_2WO_6 was prepared by calcination of a stoichiometric mixture of iron oxide and tungsten oxide [24]. The mechanically mixed catalyst (Fe_2O_3-800+Fe_2WO_6) is thought to simulate the ideal $W_{0.13}FeO_x$ catalyst with complete crystallization.

2.2 Sample characterization

X-ray diffraction (XRD) patterns were recorded on a Rigaku D/max-2500/PC diffractometer employing Cu Kα radiation (λ = 1.5418 Å) operating at 50 kV and 200 mA. The Brunauer-Emmett-Teller (BET) surface area and pore structure were measured by N_2 adsorption/desorption using a Micromeritics 2020 M instrument. Before N_2 physisorption, the sample was outgassed at 300°C for 5 h. Inductively coupled plasma-atomic emission spectrometer (ICP-AES) experiments were carried out on the IRIS Intrepid IIXSP instrument from Thermo elemental. Field emission scanning electron microscope (FESEM) was performed on a Hitachi SU-70 microscope. High-resolution transmission electron microscopy (HRTEM) equipped with selected area electron diffraction (SAED) and energy dispersive X-ray analysis (EDX) was conducted on a JEOL JEM-2010 microscope at an accelerating voltage of 200 kV. High-angle annular dark field scanning transmission electron microscopy (HAADF-STEM) images were recorded in a Tecnai F20. X-ray photoelectron spectroscopy (XPS) data were obtained on an AXIS-Ultra instrument from Kratos Analytical using monochromatic Al Kα radiation (225 W, 15 mA, 15 kV) and low-energy electron flooding for charge compensation. To compensate for surface charge effects, the binding energies were calibrated using the C 1s

hydrocarbon peak at 284.80 eV. X-ray absorption fine structure (XAFS) measurements at the W L_{III}-edge and Fe K-edge were performed in the transmission mode and fluorescence mode at room temperature on the XAFS station of the 1W1B beamline of Beijing synchrotron radiation facility (BSRF, Beijing, China), respectively. XAFS data were analyzed using IFEFFIT software package [25]. In the least-squares-fitting procedure, the possible scattering paths were also calculated using this software package.

Temperature-programmed reduction in H_2 (H_2-TPR) was performed in a quartz reactor with a thermal conductivity detector (TCD) to monitor the H_2 consumed. A 50 mg sample was pretreated *in situ* at 500^{o}C for 1 h in a flow of O_2 and cooled to room temperature in the same gas. TPR was conducted at 10^{o}C/min to 900^{o}C in a 30 mL/min flow of 5 vol.% H_2 in N_2. CuO was used as a calibration reference.

The temperature-programmed desorption of NH_3 (NH_3-TPD) experiments were performed in a quartz reactor using 50 mg catalyst. NH_3 was monitored using a quadrupole mass spectrometer (MS; OmniStar 200, Balzers) with m/z=16. Prior to the experiments, the samples were pretreated at 500^{o}C for 30 min in 10 vol% O_2/He (50 mL/min) and cooled to 100^{o}C. Sample was exposed to 0.4 % NH_3 (50 mL/min) until the outlet NH_3 concentration was stable. The samples were then purged with He to remove any weakly absorbed NH_3 and then the heated to 800^{o}C at 10^{o}C/min.

The *in situ* FTIR spectra of reaction were recorded using a Bruker Tensor 27 spectrometer over the range 4000-400 cm^{-1}, with 16 scans, at a resolution of 4 cm^{-1}. Self-supporting wafers were pretreated in the IR cell at 500^{o}C in a flow of He for 30 min to remove adsorbed species. After cooling to room temperature (RT) or 100^{o}C, the background spectrum was recorded. The IR spectra were recorded at RT or 100^{o}C in a flow of 500 ppm NH_3 + He (150 mL/min)

or 500 ppm NO + 500 ppm NH_3 + 5.3 % O_2 + He (300 mL/min). Samples were then heated to 450°C at 10°C/min.

2.3 Catalytic testing

The steady state SCR and NO oxidation activity over W_aFeO_x catalysts was tested in a fixed-bed quartz tube reactor (6.0 mm i.d.) with a thermocouple placed inside catalysts in the temperature range of 150-500°C. In the SCR reaction, the model flue gas consisting of 500 ppm NO, 500 ppm NH_3, 5.3 vol.% O_2, 10 vol.%, and balanced with He. The total flow rate maintained at 300 mL/min, corresponding to a gas hourly space velocity (GHSV) of 50000 h^{-1}. In the case of NO oxidation, the feed consisted of 500 ppm NO, and 5 vol.% O_2 with He as balance. The total flow rate kept at 100 mL/min and the same GHSV (50000 h^{-1}) was used. Concentrations of NO and NO_2 were monitored by chemiluminiscence analyzer (42*i*-HL, Thermo). N_2O and NH_3 were detected by a quadrupole mass spectrometer (MS, OmniStar 200, Balzers) using the m/z signals of 44 for N_2O, and 17 for NH_3. The data for steady-state activities of catalysts were collected after ca. 1 h on stream. The durability tests of the catalysts were performed in the SCR reaction feed at 300°C for 12 h.

The reaction rate was measured using the same conditions as for steady-state reaction. However, in this case, the powder samples were pressed, crushed and sieved (100-200 mesh) prior to use. The GHSV was estimated as 200,000 h^{-1}. Isothermal reactions at 180°C were conducted at a stable and low NO_x conversion (≤15%) ensuring operation within the kinetic regime.

3. Results and discussion

XRD patterns of W_aFeO_x show the presence of few Fe_2O_3 microcrystals in the large-scale amorphous phase [26]. Strong interaction between W and Fe in the W_aFeO_x inhibits crystallization of the individual components during the precipitation process, and results in much higher surface areas [19, 26, 27] and gives rise to the geometry and morphology changes observed (Figure 1). The 3D flower-type structure of W_aFeO_x is composed of numerous irregular nanosheets which randomly stack together. The HAADF-STEM image and corresponding elemental mapping confirmed that the W atoms are incorporated into the rhombohedral matrix of Fe_2O_3 [26].

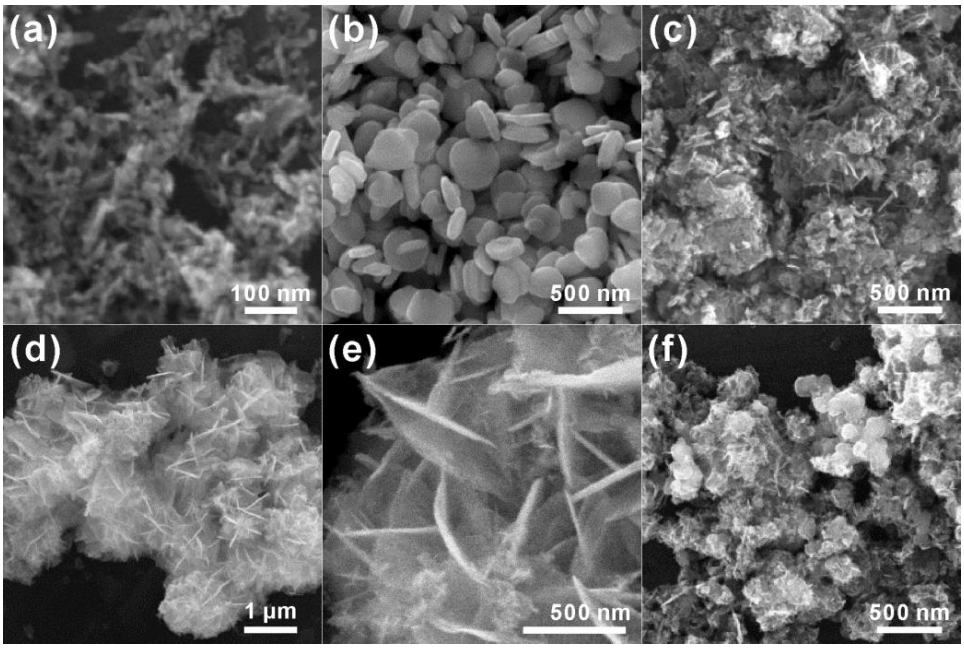

Figure 1. SEM images of W_aFeO_x catalysts: (a) Fe_2O_3, (b) WO_3, (c) $W_{0.09}FeO_x$, (d, e) $W_{0.13}FeO_x$, and (f) $W_{0.17}FeO_x$.

XAFS spectra were measured in order to obtain information about the local environment around the specific atoms in poorly-crystalline W_aFeO_x [19, 28]. The Fe K-edge XANES

spectra and RSF curves for Fe_2O_3 and W_aFeO_x are similar, indicating that the Fe atoms in W_aFeO_x are trivalent and exhibit octahedral (O_h) coordination, similar to Fe_2O_3 (Figure S1a) [26]. In the case of the W L_{III}-edge, the peak position and shape of the normalized XANES and RSF curves for W_aFeO_x correspond with those of Fe_2WO_6, which implies that most of the hexavalent W atoms in W_aFeO_x exist in the same O_h coordination environment as that of Fe_2WO_6 anions (Figure S1b and c), namely forming W-O-Fe short-range ordered structure [29]. The lower intensity of the RSF curves can be attributed to the higher local disorder level for W_aFeO_x [30]. Notably, the disordered structure is strongly reflected in the Debye-Waller factor (DWF, σ^2), a term appearing in the EXAFS equation that accounts for the level of disorder of a given sample [31, 32]. DWFs for W_aFeO_x were obtained by quantitative curve fitting in R-space of the W L_{III}-edge EXAFS spectra (Figure 2, Figure S1c and Table S1).

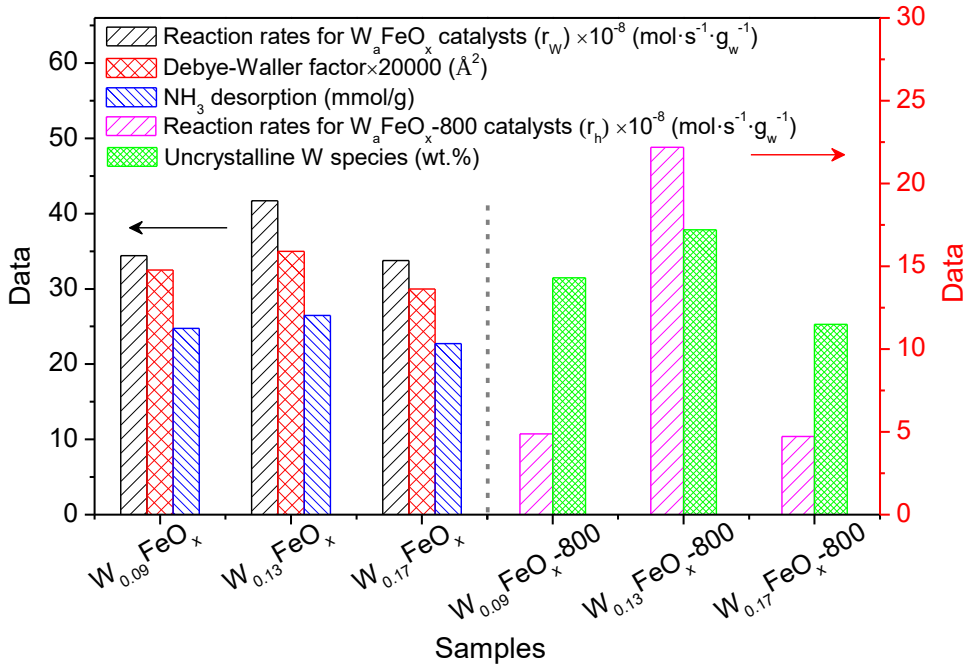

Figure 2. Reaction rates normalized by W contents (r_W), Debye-Waller factor (DWF), NH_3 adsorption amount for W_aFeO_x catalysts; reaction rates (r_h) and amount of non-crystalline W species for W_aFeO_x-800 catalysts.

In our previous studies [26], W_aFeO_x promoted NO conversion at low temperature compared with Fe_2O_3 and WO_3 due to the higher surface area and surface W/Fe atomic ratios (Table S2). In the present work, the reaction rates of W_aFeO_x normalized by W content (r_W) were measured to provide a reliable correlation between the intrinsic activity and the amount of W-containing species. As shown in Figure 2, the r_W at 180°C shows a clear positive correlation with the DWF for W_aFeO_x, suggesting that the W-O-Fe structure acts as the active sites for W_aFeO_x catalysts, as all W atoms participate in the formation of the W-O-Fe structure.

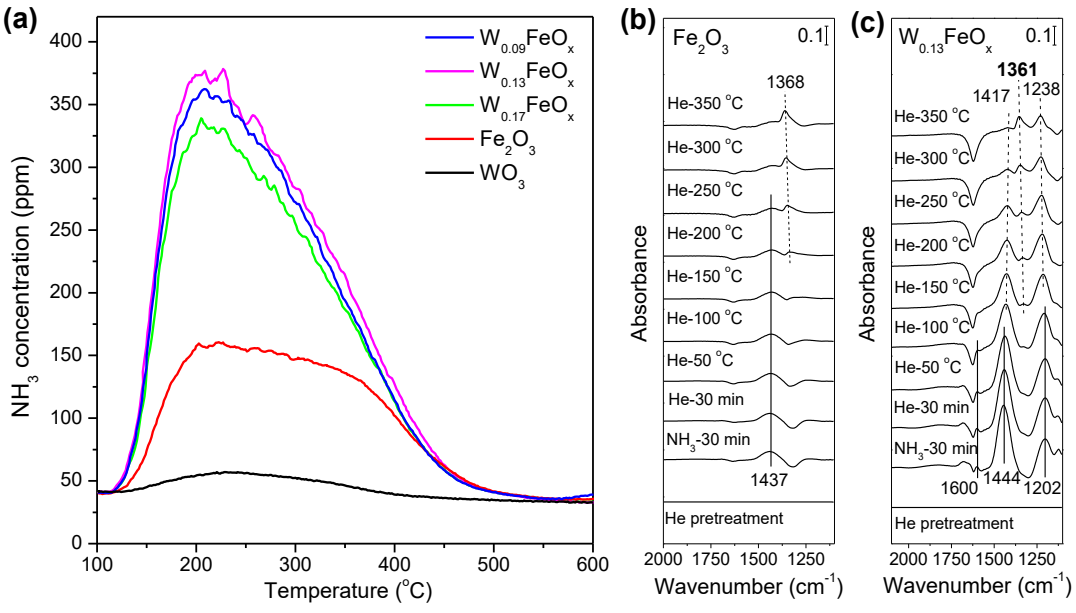

Figure 3. (a) NH_3-TPD profiles for Fe_2O_3, WO_3, and W_aFeO_x catalysts; *in situ* FTIR spectra of NH_3 exposed to (b) Fe_2O_3 and (c) $W_{0.13}FeO_x$ at room temperature and subsequently heated to 350ºC in a flow of He.

To further clarify how the chemical properties of W_aFeO_x were improved by the presence of short-range ordered W-O-Fe structures, the redox properties and acidity were assessed, as these are key characteristics associated with the SCR activity [7, 33-35]. As shown in the H_2-TPR (Figure S2), the reduction of the Fe species was delayed for W_aFeO_x in comparison with Fe_2O_3, suggestive of interactions between W and Fe [36]. On the other hand, NH_3-TPD spectra show a greater amount of ammonia desorption in the range 100-500ºC (NH_3 adsorption on WO_3 is negligible) (Figure 3a), indicating numbers of acid sites in W_aFeO_x. By using the integrated NH_3-TPD peak areas, the relative amounts of adsorbed NH_3 show a clear correlation with the reaction rates of W_aFeO_x (Figure 2), suggesting that the enhanced activity is primarily related to the enhanced acidity derived from the strong interactions in the W-O-Fe structure.

To study the nature of species adsorbed on sites within the short-range ordered W-O-Fe structure during NH_3 exposure, *in situ* FTIR spectra were collected (Figure 3b and c). Fe_2O_3 does not show evidence for Lewis acidity although Brønsted acid sites are detected (~1437 cm^{-1}, Figure 3b). The coordinated NH_3 (~1202 and 1600 cm^{-1}) suggests the presence of Lewis acidity on $W_{0.13}FeO_x$ (Figure 3c) [12]. As for Brønsted acidity, a greater intensity peak ~1440 cm^{-1} was observed for $W_{0.13}FeO_x$ than Fe_2O_3. The increase in amounts of both the Lewis and Brønsted acidity promotes catalytic activity [37-42]. With increasing temperature, both the peak intensities due to adsorption at Lewis and Brønsted acid sites decreased, with the later exhibiting lower thermal stability compared with ammonia on Lewis acid sites. The band at ~1417 cm^{-1} nearly

disappeared at 350°C, whereas the band at 1238 cm^{-1} is still clearly observed. An additional band at ~1361 cm^{-1} was observed which could be ascribed to an oxidised product of adsorbed ammonia [38, 43, 44]. These results provide persuasive evidence that the atomic-scale interaction in the short-range ordered W-O-Fe structure enhances both Lewis and Brønsted acidity of the catalysts and these are favorable for catalytic activity.

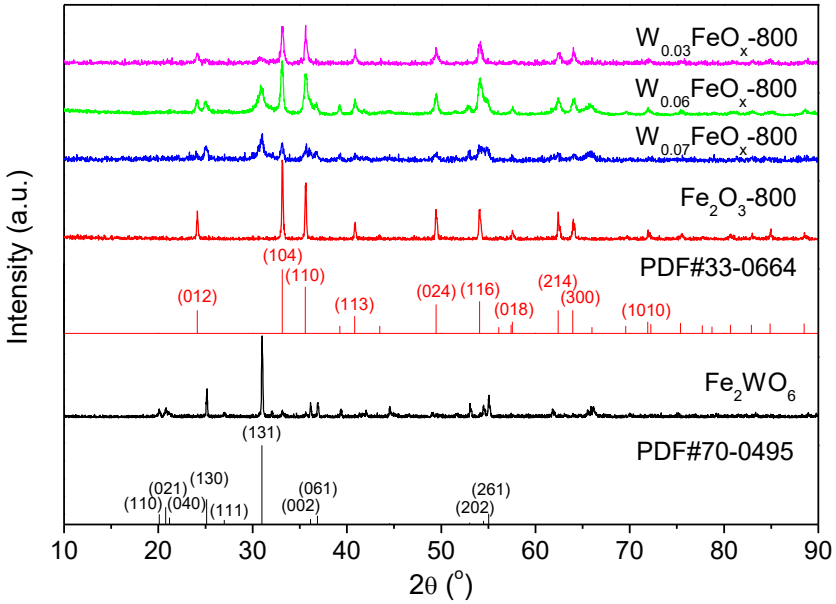

Figure 4. XRD patterns of Fe_2O_3-800, Fe_2WO_6, and W_aFeO_x-800 catalysts.

Table 1. Textural properties, XRD and ICP data of Fe_2O_3-800 and W_aFeO_x-800 catalysts.

Sample	Surface area (m^2/g)	Pore volume (cm^3/g)	Pore size (nm)	Fe_2WO_6 concentration from XRD (wt.%)	W mass concentration from ICP[26] (wt.%)	W contents in Fe_2WO_6 phase (wt.%)	Non-crystalized W contents (wt.%)
$W_{0.09}FeO_x$-800	23.7	0.0843	16.4	4.42	16.4	2.1	14.3
$W_{0.13}FeO_x$-800	20.0	0.0573	14.1	12.82	23.2	6.0	17.2

$W_{0.17}FeO_x$-800	18.3	0.0657	14.4	33.91	27.4	15.9	11.5
Fe_2O_3-800	2.5	0.0078	67.3	--	--	--	--

234

235

236 To determine the stability of the short-range ordered W-O-Fe structure at higher temperature,
237 the W_aFeO_x samples were calcined at high temperature (800°C, 5 h) (denoted as W_aFeO_x-800).
238 An increase in calcination temperature (Figure 4), results in the emergence of a new phase,
239 Fe_2WO_6 (JCPDS 70-0495) in addition to Fe_2O_3, indicating a transformation from amorphous to
240 crystalline. This confirmed the XAFS results that W in W_aFeO_x exists in the O_h coordination
241 environment as in Fe_2WO_6. From quantitative analysis of W concentrations (wt.%) in Fe_2WO_6
242 phase over different samples on the basis of XRD data, it is interesting to note that the
243 concentrations are lower than those obtained by ICP, suggesting that only a part of the
244 amorphous W-containing species in W_aFeO_x are transformed into Fe_2WO_6 crystallites, while the
245 other remains in an amorphous state (Table 1). As shown in Table 1, $W_{0.13}FeO_x$-800 possesses
246 the highest non-crystalized W content. As expected, the BET surface area was significantly
247 decreased on increasing the calcination temperature.

248 SCR performances of W_aFeO_x-800 catalysts show that the increasing calcination temperature
249 resulted only in the decrease of low-temperature activity due to the decreased BET surface area,
250 but had no clear influence on the high-temperature activity (Figure 5). Furthermore, NO_x
251 conversion for $W_{0.13}FeO_x$-800, as an example, was stable over a 12 h test period (Figure S3). The
252 high activity at 300-450°C compared with the low activity of Fe_2O_3-800 might be ascribed to
253 Fe_2WO_6 microcrystals or the synergistic effect of Fe_2O_3 and Fe_2WO_6 microcrystals. However,
254 this proposal is rejected based on the poor SCR activity of pure Fe_2WO_6 and Fe_2O_3-800+Fe_2WO_6
255 samples (Figure 5). The latter is thought to simulate the ideal $W_{0.13}FeO_x$ catalyst with complete

crystallization. It remains unanswered as to whether the retained activity is related with the residual amorphous phase and where these are located.

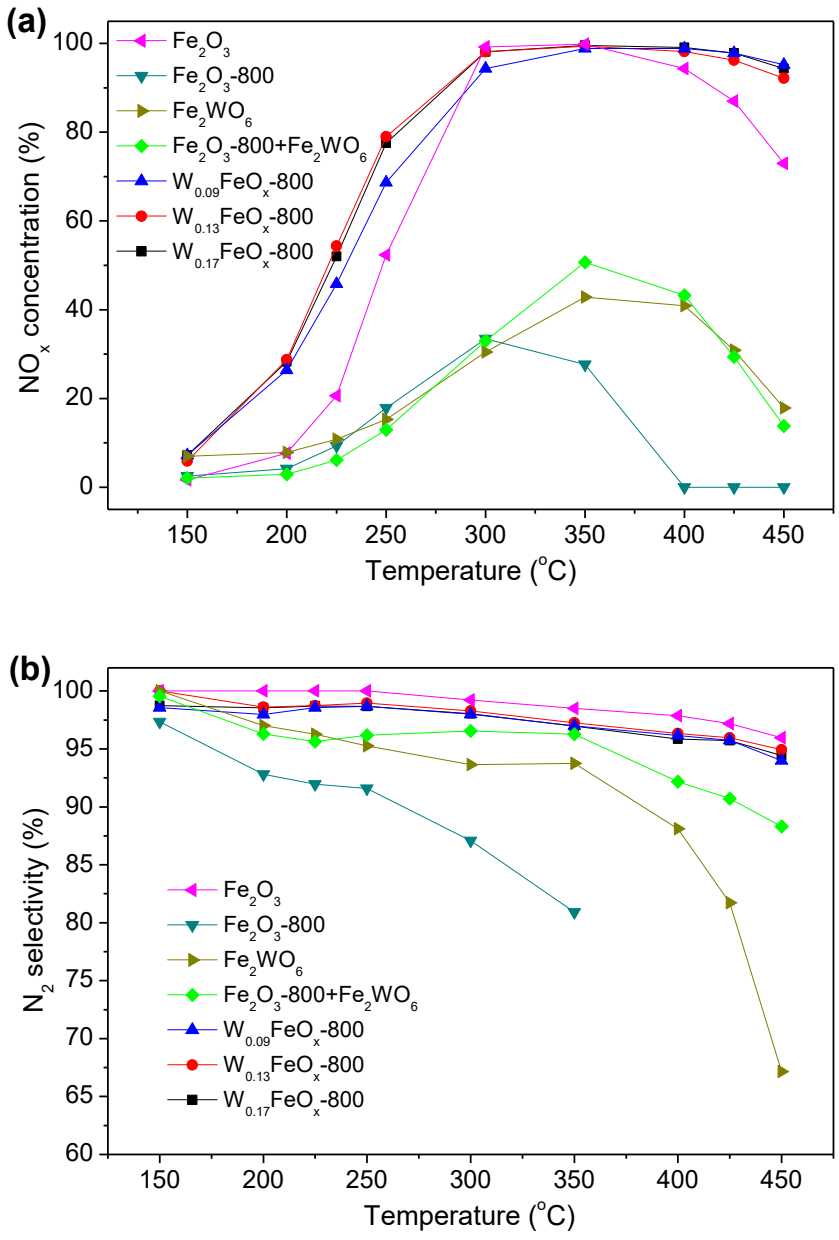

Figure 5. (a) NO_x conversion and (b) N_2 selectivity of W_aFeO_x-800 catalysts and reference samples.

Figure 6 shows TEM images for $W_{0.13}FeO_x$-800. The well-crystallized Fe_2O_3 and Fe_2WO_6 microcrystals are randomly aggregated for $W_{0.13}FeO_x$-800 (Figure 6a). Based on the extensive characterization, the Fe_2WO_6 phase consists of long-range ordered W-O-Fe structures, which are derived from the sintering of the coordinated W, O, and Fe atoms in amorphous phase (Figure S4). HRTEM was used to provide directly interpretable images of W_aFeO_x-800 to search for the remaining amorphous phases (Figure 6b-d). Surprisingly, an amorphous phase layer of ~2 nm thickness was detected on the surfaces of Fe_2WO_6 and Fe_2O_3 microcrystals for $W_{0.13}FeO_x$-800. According to the semi-quantitative analysis of surface atomic concentrations (% as molar ratio) over $W_{0.13}FeO_x$-800 from XPS data, the surface W/Fe atomic ratio was 0.48, which is much higher than the surface and bulk ratios for $W_{0.13}FeO_x$ (XPS and ICP data [26], respectively, Table S2), suggesting an enrichment of amorphous W-containing species on the surface.

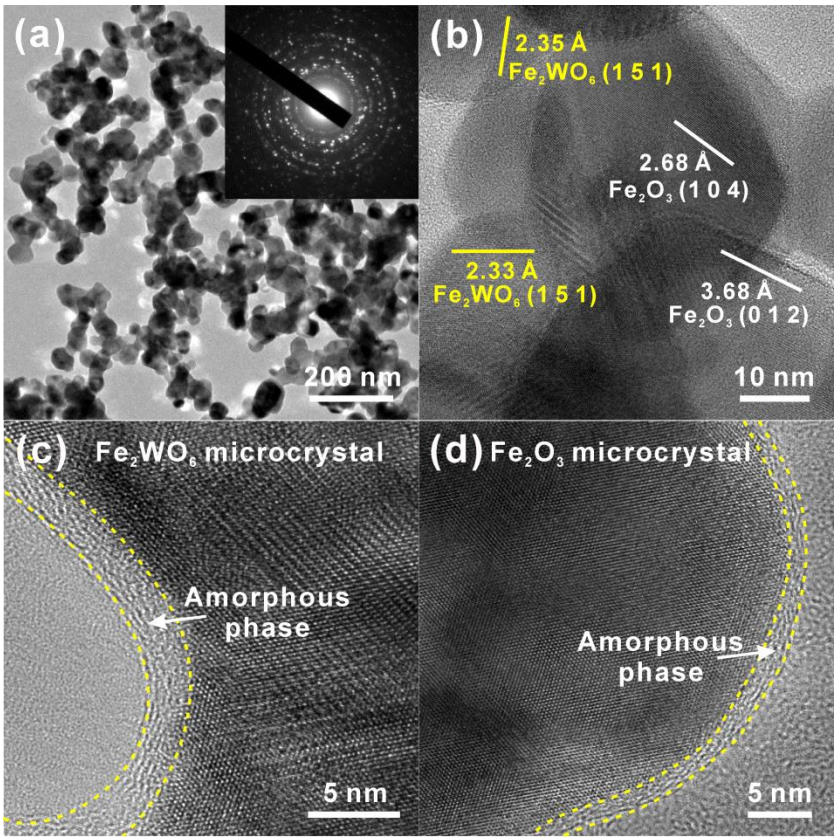

Figure 6. (a) TEM images with SAED patterns (insets), (b-d) HRTEM images for $W_{0.13}FeO_x$-800.

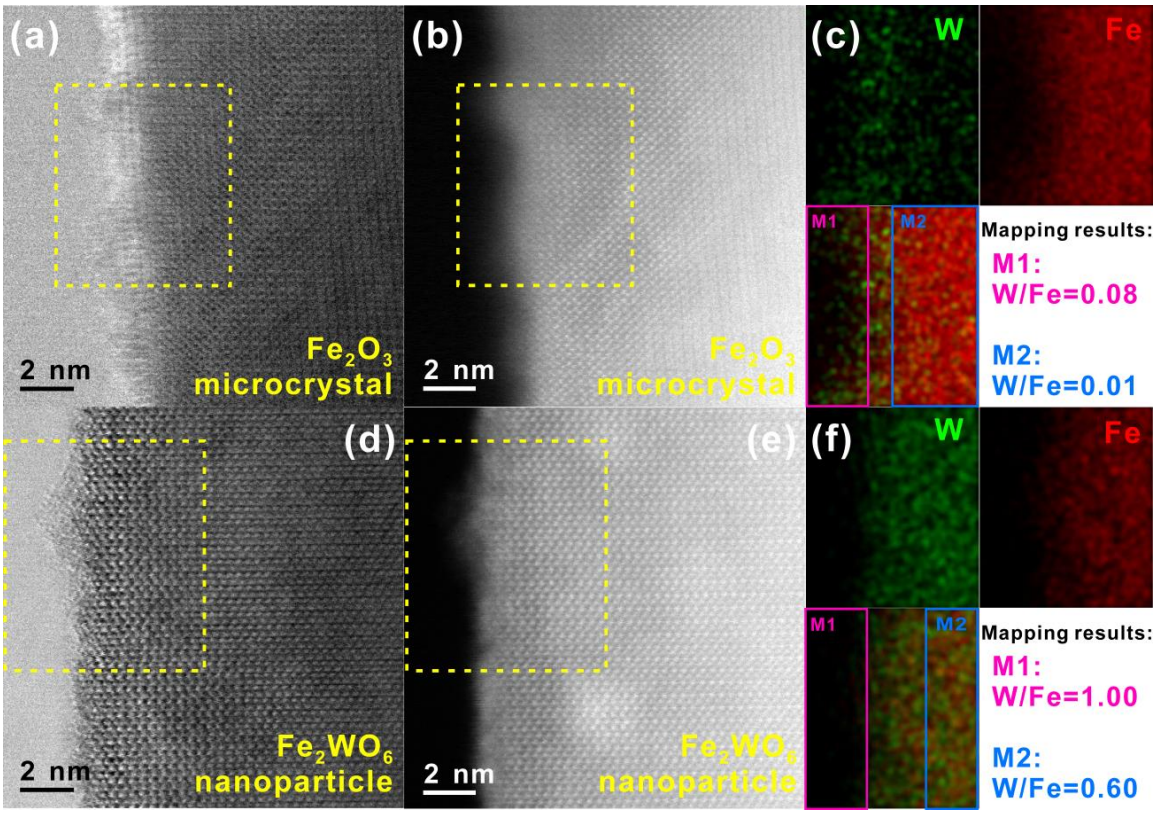

Figure 7. HRTEM images and EDX analysis of Fe_2O_3 and Fe_2WO_6 nanoparticles in $W_{0.13}FeO_x$-800 catalyst: (a) HRTEM bright-field image, (b) HAADF image, and (c) EDX mapping results of the region in the yellow dashed box for a Fe_2O_3 nanoparticle; (d) HRTEM bright-field image (e) HAADF image, and (f) EDX mapping results of the region in the yellow dashed box for a Fe_2WO_6 nanoparticle.

The chemical composition of the amorphous overlayer was determined by HAADF-STEM in conjunction with the corresponding EDX mappings (Figure 7). The latter was acquired from both the overlayer and the inside of Fe_2O_3 and Fe_2WO_6 nanoparticles. HAADF-STEM clearly

shows that the Fe atoms are homogeneously distributed over the Fe_2O_3 nanoparticle, while the W atoms are detected primarily on the surface of the amorphous overlayers of the Fe_2O_3 nanoparticles (Figure 7a-c). EDX gives a W/Fe molar ratio of about 0.08 for the amorphous overlayer on the Fe_2O_3 nanoparticle, which is much higher than that in the Fe_2O_3 nanoparticle (0.01), suggesting that W atoms are primarily doped in the amorphous Fe-O overlayer of the Fe_2O_3 nanoparticle (Figure 7a-c), with similar short-range ordered W-O-Fe structure as in W_aFeO_x. Comparatively, HAADF-STEM images of the Fe_2WO_6 nanoparticle show Fe and W atoms throughout the whole section (Figure 7d-f). EDX indicates that the W/Fe molar ratio of the overlayer on the Fe_2WO_6 nanoparticle is 1.00, consistent with that of the short-range ordered W-O-Fe structure. On extending to the inside of the Fe_2WO_6 nanoparticle, the W/Fe molar ratio decreases to 0.60, which is very close to that of the bulk Fe_2WO_6. The above analysis confirms that the non-crystallized W species as derived from XRD are mainly located in the amorphous overlayers of the Fe_2O_3 and Fe_2WO_6 nanoparticles, which agrees well with the XPS. Consequently, the retained high-temperature activity of W_aFeO_x-800 is a consequence of the amorphous phase on the surface of microcrystals.

Following the same strategy as applied to W_aFeO_x, the reaction rates (r_h) of W_aFeO_x-800 were also measured (Figure 2). Apparently, the variation of r_h correlates well with the amount of amorphous W-containing species (Figure 2 and Table 1), providing proof that the intrinsic activity was derived from the W-O-Fe structure on the surface amorphous overlayer. In other words, the short-range ordered W-O-Fe active sites in W_aFeO_x were retained in the W_aFeO_x-800 in the form of the surface amorphous overlayer, which ensures retained the high-temperature activity at 300-450^{o}C after aging at 800^{o}C for 5 h.

4. Conclusions

Poorly-crystalline W-Fe composite oxides (W_aFeO_x), consisting of short-range ordered W-O-Fe structures were prepared. A direct correlation between the level of disorder and the intrinsic activity indicated that the short-range ordered W-O-Fe structure hosts the active catalytic sites. Strong atomic-level interactions between Fe and W atoms within the disordered W-O-Fe structure was shown and this enhanced the amounts of Lewis and Brønsted acidity, leading to improved deNO_x activity. Of significance, the short-range ordered W-O-Fe structure was retained as amorphous overlayers over the surface of crystalline particles after aging at 800^{o}C for 5 h, leading to the retention of activity. This finding may open up new pathways in the fabrication of the active deNO_x catalysts with high thermal stability by rationally enhancing atomic-scale interactions between heteroatoms in composite oxides.

Acknowledgements

This work was supported by National Natural Science Foundation of China (No. 21477046, 21333003, and 21673072) and Key Technology R&D Program of Shandong Province (No. 2016ZDJS11A03).

References

[1] H. Bosch, F. Janssen, Catal. Today 2 (1988) 369-532.

[2] M.V. Twigg, Appl. Catal. B: Environ.70 (2007) 2-15.

[3] G. Busca, L. Lietti, G. Ramis, F. Berti, Appl. Catal. B: Environ. 18 (1998) 1-36.

[4] J.H. Li, H.Z. Chang, L. Ma, J.M. Hao, R.T. Yang, Catal. Today 175 (2011) 147-156.

[5] S. Brandenberger, O. Kröcher, A. Tissler, R. Althoff, Catal. Rev. 50 (2008) 492-531.

[6] Z.G. Liu, N.A. Ottinger, C.M. Cremeens, Atmos. Environ. 104 (2015) 154-161.

[7] F.D. Liu, Y.B. Yu, H. He, Chem. Commun. 50 (2014) 8445-8463.

[8] E. Curry-Hyde, A. Baiker, Ind. Eng. Chem. Res. 29 (1990) 1985-1989.

[9] H.E. Curry-Hyde, H. Musch, A. Baiker, Appl. Catal. 65 (1990) 211-223.

[10] X.L. Tang, J.M. Hao, W.G. Xu, J.H. Li, Catal. Commun. 8 (2007) 329-334.

[11] P.G. Smirniotis, D.A. Peña, B.S. Uphade, Angew. Chem. Int. Ed. 40 (2001) 2479-2482.

[12] D.A. Peña, B.S. Uphade, P.G. Smirniotis, J. Catal. 221 (2004) 421-431.

[13] W.Q. Xu, Y.B. Yu, C.B. Zhang, H. He, Catal. Commun. 9 (2008) 1453-1457.

[14] X. Gao, Y. Jiang, Y. Zhong, Z.Y. Luo, K.F. Cen, J. Hazard. Mater. 174 (2010) 734-739.

[15] X. Gao, Y. Jiang, Y.C. Fu, Y. Zhong, Z.Y. Luo, K.F. Cen, Catal. Commun. 11 (2010) 465-469.

[16] F.D. Liu, H. He, C.B. Zhang, Chem. Commun. (2008) 2043-2045.

[17] F.D. Liu, H. He, Y. Ding, C.B. Zhang, Appl. Catal. B: Environ. 93 (2009) 194-204.

[18] F.D. Liu, H. He, C.B. Zhang, Z.C. Feng, L.R. Zheng, Y.N. Xie, T. D. Hu, Appl. Catal. B: Environ. 96 (2010) 408-420.

[19] P. Li, Y. Xin, Q. Li, Z.P. Wang, Z.L. Zhang, L.R. Zheng, Environ. Sci. Technol. 46 (2012) 9600-9605.

[20] Y. Peng, K.Z. Li, J.H. Li, Appl. Catal. B: Environ. 140-141 (2013) 483-492.

[21] D.A. Drabold, Eur. Phys. J. B 68 (2009) 1-21.

[22] D.L. Cocke, Int. J. Min. Met. Mater. 38 (1986) 70-75.

[23] B. Guan, R. Zhan, H. Lin, Z. Huang, Appl. Therm. Eng. 66 (2014) 395-414.

[24] J.J. Pak, M. Bahgat, M.K. Paek, J. Alloy. Compd. 477 (2009) 357-363.

[25] M. Newville, J. Synchrotron Radiat. 8 (2001) 322-324.

[26] Y. Xin, N.N. Zhang, Q. Li, Z.L. Zhang, X.M. Cao, L.R. Zheng, Y.W. Zeng, J.A. Anderson, ACS Catal. (2018) DOI: 10.1021/acscatal.7b02638.

[27] B.M. Reddy, A. Khan, Catal. Rev. 47 (2007) 257-296.

[28] D. C. Koningsberger, R. Prins, Trac-Trend. Anal. Chem. 1 (1981) 16-21.

[29] S. Yamazoe, Y. Hitomi, T. Shishido, T. Tanaka, J. Phys. Chem. C 112 (2008) 6869-6879.

[30] L.S. Cavalcante, M.A.P. Almeida, W.A. Jr., R.L. Tranquilin, E. Longo, N.C. Batista, V.R. Mastelaro, M.S. Li, Inorg. Chem. 51 (2012) 10675-10687.

[31] B.K. Teo, EXAFS: Basic principles and data analysis. Springer-Verlag: Berlin, 1986.

[32] Z.M. Qi, C.S. Shi, Y.G. Wei, Z. Wang, T. Liu, T.D. Hu, Z.Y. Zhao, F.L. Li, J. Phys.: Condens. Matter 13 (2001) 11503-11509.

[33] S.J. Yang, J.H. Li, C.Z. Wang, J.H. Chen, L. Ma, H.Z. Chang, L. Chen, Y. Peng, N.Q. Yan, Appl. Catal. B: Environ. 117-118 (2012) 73-80.

[34] J.P. Chen, R.T. Yang, Appl. Catal. A: Gen. 80 (1992) 135-148.

[35] R.K. Grasselli, A.W. Sleight, Structure-activity and selectivity relationships in heterogeneous catalysis. Elsevier: New York, 1991.

[36] K. Arakawa, S. Matsuda, H. Kinoshita, Appl. Surf. Sci. 121-122 (1997) 382-386.

[37] R.Q. Long, R.T. Yang, J. Catal. 207 (2002) 224-231.

[38] Q. Li, H.C. Gu, P. Li, Y.H. Zhou, Y. Liu, Z.N. Qi, Y. Xin, Z.L. Zhang, Chin. J. Catal. 35 (2014) 1289-1298.

[39] R.Q. Long, R.T. Yang, J. Catal. 190 (2000) 22-31.

[40] M.A. Larrubia, G. Ramis, G. Busca, Appl. Catal. B: Environ. 27 (2000) L145-L151.

[41] S.D. Lin, A.C. Gluhoi, B.E. Nieuwenhuys, Catal. Today 90 (2004) 3-14.

[42] Y. Shu, H. Sun, X. Quan, S. Chen, J. Phys. Chem. C 116 (2012) 25319-25327.

[43] Z.M. Liu, H. Su, J.H. Li, Y. Li, Catal. Commun. 65 (2015) 51-54.

[44] L. Chen, J.H. Li, W. Ablikim, J. Wang, H.Z. Chang, L. Ma, J.Y. Xu, M.F. Ge, H. Arandiyan, Catal. Lett. 141 (2011) 1859-1864.